High-Resolution Ultrasound Imaging Using Random Interference

Pavel Ni, *Student Member, IEEE*, and Heung-No Lee, *Senior Member, IEEE*

***Abstract*— Spatial resolution in conventional sonography is achieved through focusing and steering of an ultrasound beam. However, due to acoustic diffraction, the ability to focus an ultrasound beam is limited which leads to low spatial and contrast resolutions. We aim to propose a new method wherein the array elements are simultaneously excited with signals coded with random sequences, which yields an unfocused ultrasound wavefront of random interference. When such a wavefront propagates through the medium, its energy reflects back from the tissue, causing individual scatterers to have unique impulse responses. In such a case, we can reconstruct high-resolution ultrasound images using *a priori* measurements of spatial impulse responses and the l_1-norm minimization algorithm. In a simulation study, we achieved a spatial resolution of 0.25 mm, which constitutes a four-fold improvement over conventional methods that use delay-and-sum beamforming. In the experimental study, we demonstrate the accuracy of the proposed interference-based method using a tissue-mimicking phantom with 0.1- and 0.08-mm-diameter nylon wires.**

***Index Terms*— Array signal processing, compressed sensing, high-resolution imaging, image reconstruction, ultrasonic imaging.**

I. Introduction

THE ultrasound is widely accepted as the preferred diagnostic imaging modality. Sonography works according to the pulse-echo principle: an incident ultrasound wave is transmitted into a medium in which waves are partially reflected back to an array of transducers. Subsequently, the signals received at the array are processed to create the final ultrasound image. The resolution in ultrasound imaging varies spatially and depends on parameters such as frequency of the transmitted signal, beamwidth, size of the aperture, and transmit focal depth. These parameters restrict the ability to focus the ultrasound waves, thus imposing a physical limitation on the final resolution. Similar to optical imaging, ultrasound resolution is defined by the diffraction limit [1]. The theoretical spatial resolution in ultrasound imaging, for a single-cycle pulse, is equal to half the acoustic wavelength [2]. However, the best axial and lateral resolution is several times lower than the diffraction limit due to high ultrasound attenuation and speckle noise [3]. Achieving a resolution beyond these limits would significantly improve the accuracy of medical diagnosis.

The components of ultrasound resolution can be classified into detail, contrast, and temporal. Various methods have been proposed in the past few decades to improve the image quality in ultrasound systems. For example, enhanced detail and contrast resolution were achieved with the introduction of multielement transducer arrays and phased arrays [4]. These array types enable advanced beamforming techniques such as plane-wave imaging [5], synthetic transmit aperture (STA) [6], and dynamic focusing [7]. Various filtering techniques have been developed to suppress speckle noise [8], [9]. Coded excitation has been used to achieve extended imaging depth [10]. Other excitation sequences have also been investigated; for example, a delay-encoded transmission scheme was proposed in [11] to increase the signal-to-noise ratio (SNR). Such methods can improve image quality; however, the resolution remains limited by the diffraction.

Several works have used compressive sensing (CS) theory [12]–[14] to prove the effectiveness of some ultrasound applications. For example, a sub-Nyquist sampling scheme based on CS was proposed in [15] to speed up data acquisition. In [16], a beamforming process was integrated directly into the sub-Nyquist sampling scheme, which yielded an even higher temporal resolution. Likewise, the schemes proposed in [17]–[19] reduce the computational cost of using different subsampling schemes. In [20], CS was applied to STA imaging to reduce the number of firings, which can potentially increase the system frame rate. In [21], a CS framework derived from the ultrasound propagation theory was introduced to reconstruct the complete ultrasound image from the transmission of a single plane wave. Such methods can increase temporal resolution at the cost of computationally complex algorithms.

"Super-resolution" refers to an imaging technique that is capable of imaging objects smaller than the initial wavelength of the transmitted ultrasound signal. Multiple studies have demonstrated the feasibility of super-resolution techniques in ultrasound imaging. For example, in [22]–[24], different techniques were proposed to visualize microvessels and blood flow speed estimation using contrast agents such as microbubbles. However, super-resolution techniques that can be used without contrast agents are limited in acoustic imaging due

Manuscript received December 29, 2019; accepted April 4, 2020. Date of publication April 8, 2020; date of current version August 27, 2020. This work was supported in part by the National Research Foundation of Korea (NRF) Grant funded by the Korean Government (MSIP) under Grant NRF-2018R1A2A1A19018665. *(Corresponding author: Heung-No Lee.)*

The authors are with the Department of Electrical Engineering and Computer Science, Gwangju Institute of Science and Technology, Gwangju 61005, South Korea (e-mail: heungno@gist.ac.kr).

Digital Object Identifier 10.1109/TUFFC.2020.2986588

to high attenuation and the distortion of backscattered signals. A promising super-resolution technique was proposed in [25], which uses a back-projection approach to visualize objects that are entirely within the ultrasound beam.

Recently, advanced statistical and signal processing techniques have allowed the development of imaging methods that are radically different from our traditional understanding of imaging [26]. Such imaging modalities utilize intentionally created randomness in the image acquisition process. For example, an optical imaging setup based on the propagation of light through a multiply scattering medium was proposed in [27]. Similarly, an imaging scheme based on a turbid medium to achieve a high acceptance angle was proposed in [28] and [29]. In [30], CS 3-D imaging using a single element was introduced to simplify the hardware design. Such methods extend the boundaries of imaging beyond the existing limits. However, improving ultrasound resolution using methods based on random signal acquisition remains a challenging task due to high signal attenuation and limited transducer bandwidth.

In this article, we demonstrate a new interference-based method that improves the spatial resolution of ultrasound imaging systems. We propose using a novel unfocused transmission of excitation signals coded with pseudorandom sequences that yield an incident wavefront of random interference. The received echo signals are the result of multiple reflections of the incident ultrasound wavefront from the scatterers. High-resolution ultrasound images are reconstructed using the *a priori* measurements of spatial impulse responses of individual point scatterers and an l_1-norm minimization algorithm. An ultrasound research system has been developed that is capable of generating a wavefront of random interference. The feasibility of the proposed method has been tested using numerical simulations and real phantom experiments.

The remainder of this article is organized as follows. In Section II, we describe the proposed interference-based method using a linear acoustic model and present the image reconstruction scheme based on the l_1-norm minimization algorithm. In Section III, we provide simulation and experimental results. Finally, in Section IV, we compare our results with recently published literature and summarize the contributions of this work.

II. Interference-Based Imaging

In conventional ultrasound imaging, beamforming is usually used to focus ultrasound waves. However, due to acoustic diffraction, the ability to focus an ultrasound beam is limited, which leads to low spatial and contrast resolutions. We show that the resolution of ultrasound systems can be significantly improved if we transmit the proposed ultrasound wavefront of random interference instead of a focused ultrasound beam.

Fig. 1 shows a schematic illustration of the proposed imaging method. First, the incident ultrasound wavefront is generated by exciting elements of the transducer array using signals coded with random sequences. In these circumstances, individual array elements emit ultrasound waves corresponding to the applied excitation signals. All emitted waves collectively yield a complex ultrasound wavefront of constructive and destructive interference, which we simply named random interference. Traditionally, interference in ultrasound imaging is treated as an undesirable effect that degrades image quality and creates speckle noise. However, in our proposed work, we aim to utilize random interference and intentionally cause spatial impulse responses of individual point scatterers to be mutually incoherent. Under such an effort, we can recover high-resolution images using both the *a priori* measurements of spatial impulse responses and the l_1-norm minimization algorithm. The effect of random ultrasound fields has been previously studied [31]–[33].

A. System Description

In this section, we describe the proposed interference-based ultrasound system using the linear acoustic model [34], which uses spatial impulse responses as a basis to derive ultrasound echo signals. Throughout this article, we will denote vectors using bold lower-case letters and matrices using bold upper-case letters.

Let us consider the pulse-echo ultrasound system shown in Fig. 2. We consider a linear transducer array with N_{Tx} identical array elements. During transmission, all N_{Tx} elements of the transducer array are simultaneously excited with random signals. During the reception, the same transducer array is used to record the reflected ultrasound signals. We let $\mathbf{r}_j$, $\mathbf{r}_i$ be the vectors in 3-D space. We use $\mathbf{r}_j$ for each $j \in \{1, 2, \ldots, N_{\mathrm{Tx}}\}$ to indicate the position of the jth transmitting element. Likewise, the vector $\mathbf{r}_i$ for each $i \in \{1, 2, \ldots, N_{\mathrm{Rx}}\}$ indicates the position of the ith receiving element. Similarly, we let the vector $\mathbf{r}_k$ for each $k \in \{1, 2, \ldots, N_{\mathrm{Sc}}\}$ be the 3-D vector which indicates the position of the kth scatterer on the virtual grid. Thus, there are a total of N_{Sc} scatterers.

We define an ultrasound echo signal reflected off a single scatterer and received at the ith array element as follows:

$$p_{\mathrm{single}}(\mathbf{r}_i, t) = v(t) \underset{t}{\otimes} f(\mathbf{r}_k) \underset{r}{\otimes} h(\mathbf{r}_k, \mathbf{r}_i, t) \tag{1}$$

where $v(t)$ is the oscillation of transducer array (i.e., the proposed random excitation signals); $f(\mathbf{r}_k)$ is the signal of interest at the location $\mathbf{r}_k$; and $h(\mathbf{r}_k, \mathbf{r}_i, t)$ is the pulse-echo impulse response of the transducer array. We denote the spatial and temporal convolutions using $\underset{r}{\otimes}$ and $\underset{t}{\otimes}$, respectively.

When the ultrasound wavefront travels through the medium, it is scattered and reflected off a volumetric object within which the density and the propagation velocity differ from those of the surroundings. The signal $f(\mathbf{r}_k)$ of a single scatter object at the location $\mathbf{r}_k$ in (1) is defined as follows:

$$f(\mathbf{r}_k) = \frac{\Delta\rho(\mathbf{r}_k)}{\rho_0} - \frac{2\Delta c(\mathbf{r}_k)}{c_0} \tag{2}$$

where ρ_0 is the mean density of the medium, c_0 is the speed of sound in the medium, $\Delta\rho$ is the change in density, and Δc is the change in speed at the location $\mathbf{r}_k$. Here, $f(\mathbf{r}_k)$ represents the signal that we aim to reconstruct from the echo signal $p_{\mathrm{single}}(\mathbf{r}_i, t)$ (1). Equation (1) indicates how the signal of interest $f(\mathbf{r}_k)$ is observed at a receiving element such that it is blurred by the pulse-echo spatial impulse response of the array $h(\mathbf{r}_k, \mathbf{r}_i, t)$ and the transducer oscillation $v(t)$.

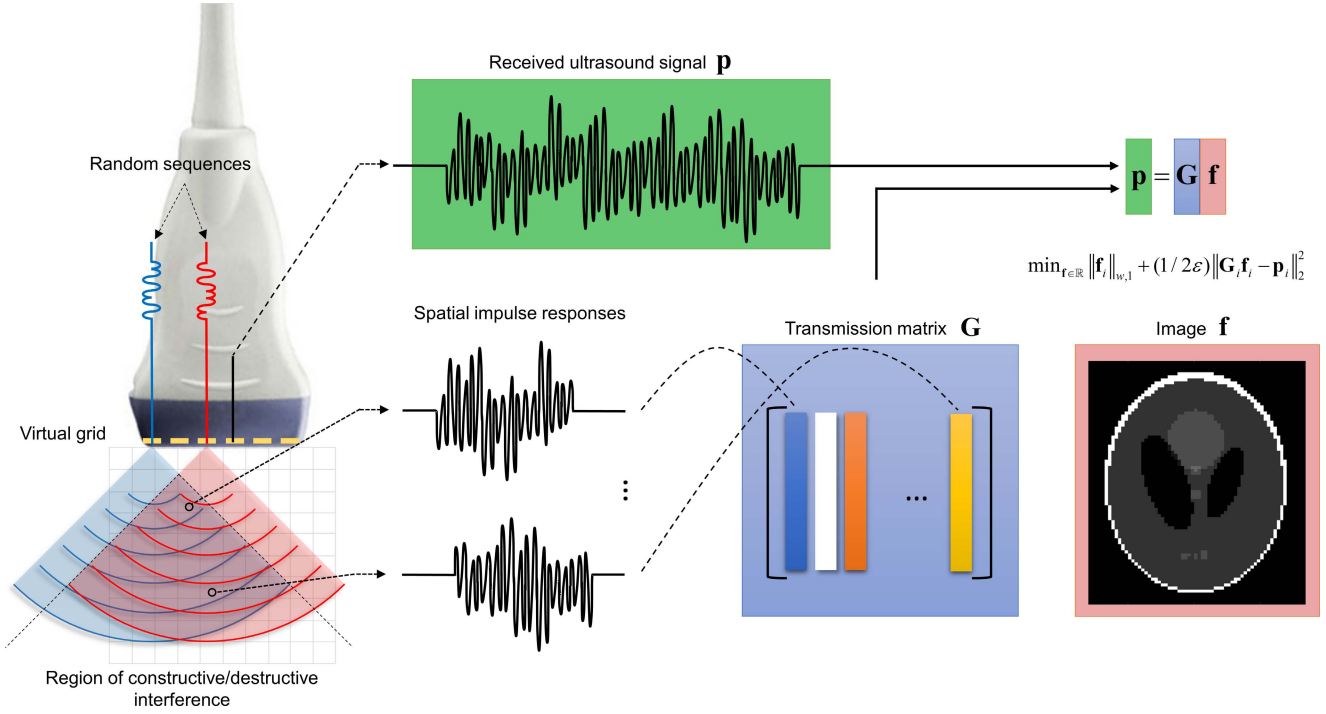

Fig. 1. System description of the proposed method. The elements of the linear transducer are excited with random signals. The transmitted wavefront has a spatially randomized pressure distribution due to the interference of several ultrasound waves. The columns of the transmission matrix are derived from the spatial impulse response of individual points on the virtual grid. Owing to the effect of interference of random signals, the spatial impulse responses have low mutual coherence. The high-resolution ultrasound images can be reconstructed from received ultrasound echo signals and the transmission matrix.

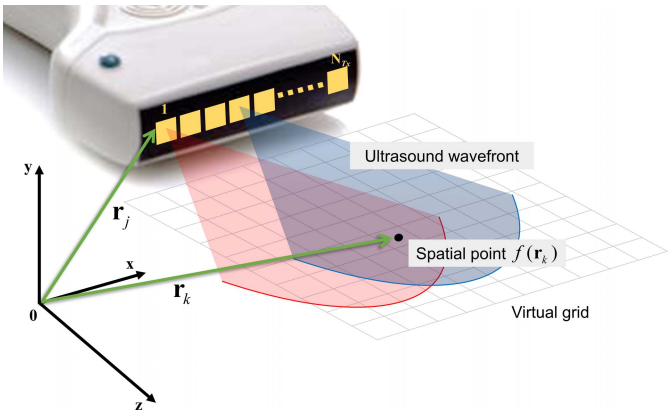

Fig. 2. Illustration of an acoustic system model.

The oscillation $v_j(t)$ of the jth transmit element $\mathbf{r}_j$ in (1) is expressed as follows:

$$v_j(t) = \frac{\rho}{2c^2} E_m(t) \underset{t}{\otimes} \frac{\partial^3 w_j(t)}{\partial t^3} \tag{3}$$

where $E_m(t)$ is an electro-mechanical response from the transducer; $w_j(t)$ for each $j \in \{1, 2, \ldots, N_{\mathrm{Tx}}\}$ corresponds to the excitation signal applied to the jth transmit element. In this article, we propose a new imaging method which requires echo signals reflected from individual point scatterers to be mutually incoherent. The incoherency is obtained by controlling the ultrasound wavefront of random interference. A wavefront of random interference can be generated by exciting each array element with a transmitting signal coded with a random sequence (see $w_j(t)$ in Section II-C). Once emitted, all the random excitation signals $w_j(t)$'s constructively and destructively interfere with each other and produce random interference.

To derive a received ultrasound echo signal, we need to find the pulse-echo impulse response $h(\mathbf{r}_k, \mathbf{r}_i, t)$ of the array. We define the pulse-echo impulse response of the array as follows:

$$h(\mathbf{r}_k, \mathbf{r}_i, t) = \sum_{j=1}^{n} h_{\mathrm{Tx}}(\mathbf{r}_k, \mathbf{r}_j, t) \underset{t}{\otimes} h_{\mathrm{Rx}}(\mathbf{r}_i, \mathbf{r}_k, t) \tag{4}$$

where h_{Tx} is the impulse response of the transmitting transducer array and h_{Rx} is the impulse response of the receiving transducer array. In the proposed method, all N_{Tx} elements of the transducer array are simultaneously excited with random signals. The impulse responses h_{Tx} and h_{Rx} are found from

$$h(\mathbf{r}_1, \mathbf{r}_2, t) = \int_S \frac{\delta(t - (|\mathbf{r}_1 - \mathbf{r}_2|/c))}{2\pi |\mathbf{r}_1 - \mathbf{r}_2|} dS \tag{5}$$

where $\mathbf{r}_1$ is the location of observation and $\mathbf{r}_2$ is the origin of the ultrasound wave. The pulse-echo impulse response (4) is the function of the relative distances from each transmitting element $\mathbf{r}_j$, for each $j \in \{1, 2, \ldots, N_{\mathrm{Tx}}\}$, to the scatterer at the spatial point $\mathbf{r}_k$, and back to the receiver at $\mathbf{r}_i$. The integral over the transducer surface, S, denotes Huygens' principle.

B. Image Reconstruction

Let us consider the region of interest (ROI) from 35 to 55 mm in the axial direction and from −10 to 10 mm in the

lateral direction. We define an ultrasound image as a collection of scatterers on a virtual grid, as shown in Fig. 2. If we define scatterers in the ROI at equal distance, $d = 0.25$ mm, then we obtain a square region with 81 points in the axial and the lateral directions and a total of $N_{\text{Sc}} = 6561$ point scatterers. To simplify this, we represent a group of scatterers on the virtual grid as a vector, $\mathbf{f} := [f(\mathbf{r}_1)\ f(\mathbf{r}_2)\ \cdots\ f(\mathbf{r}_{N_{\text{Sc}}})]$.

We use (1) to find the echo signal reflected from a single scatterer at $\mathbf{r}_k$. In our simulation, we assume that the propagation of ultrasound waves is linear; thus, we can find echo signals reflected from a group of scatterers, $\mathbf{f}$, by measuring the impulse responses of individual scatterers and summing them together. Then, the echo signal reflected from a group of scatterers is given by

$$\begin{aligned} p_{\text{group}}(\mathbf{r}_i, t) &= \sum_{k=1}^{N_{\text{Sc}}} p_{\text{single}}(\mathbf{r}_i, t) \\ &= \sum_{k=1}^{N_{\text{Sc}}} v(t) \underset{t}{\otimes} f(\mathbf{r}_k) \underset{r}{\otimes} h(\mathbf{r}_k, \mathbf{r}_i, t). \end{aligned} \tag{6}$$

Using matrix and vector notation, we can express (6) as follows:

$$\mathbf{p}_i = \mathbf{G}_i \mathbf{f}_i \tag{7}$$

where $\mathbf{p}_i \in \mathbb{R}^M$ is the column vector representation of a received ultrasound signal, $\mathbf{G}_i \in \mathbb{R}^{M \times N_{\text{Sc}}}$ is the transmission matrix, and $\mathbf{f}_i \in \mathbb{R}^{N_{\text{Sc}}}$ is a vectorized object image. Here, M is the number of signal samples and N_{Sc} is the total number of point scatterers. The echo signal $\mathbf{p}_i$ at the ith receiving element is the summation of spatial impulse responses reflected off the scatterers in the ROI. The elements of $\mathbf{f}$ represent the scattering strength of the corresponding spatial point.

In the simulation study, the transmission matrix $\mathbf{G}_i$ is generated from *a priori* measurement of spatial impulse responses obtained in Field II ultrasound software [35], [36]. The columns of the matrix $\mathbf{G}_i := [\mathbf{g}_{i,1}\ \mathbf{g}_{i,2}\ \mathbf{g}_{i,3}\ \cdots\ \mathbf{g}_{i,N_{\text{Sc}}}]$ represent the spatial responses of individual scatterers, that is, $\mathbf{g}_{i,k} := p_{\text{single}}(\mathbf{r}_i, t)$. In the experimental study, we propose generating transmission matrices from the measurements of random excitation signals obtained in a water tank experiment. The detailed procedures used to generate the transmission matrices for the experimental study are given in Section II-E.

According to the linear property of the proposed imaging system, any echo signal $\mathbf{p}_i$ of an object image $\mathbf{f}_i$ in (7) can be represented as a combination of columns of the matrix $\mathbf{G}_i$. In our ultrasound imaging model, we need to reconstruct the unknown object image $\mathbf{f}_i$ given the echo signal $\mathbf{p}_i$ and transmission matrix $\mathbf{G}_i$. The reconstruction quality of object image $\mathbf{f}_i$ improves with increasing incoherence of the responses of the point scatterers. To make the spatial impulse responses more incoherent, we propose using unfocused transmission of random excitation signals (see Section II-C). Then, we can reconstruct the image $\hat{\mathbf{f}}_i$ from solving the following optimization problem:

$$\hat{\mathbf{f}}_i := \arg\min_{\mathbf{f}} \|\mathbf{f}_i\|_1 \quad \text{subject to } \|\mathbf{G}_i \mathbf{f}_i - \mathbf{p}_i\|_2^2 \le \varepsilon \tag{8}$$

where $\|\cdot\|_1$ denotes the l_1-norm and $\varepsilon \ge 0$ is a regularization value. We use the l_1-norm minimization algorithm which can provide reliably accurate estimation for sparsely representable signals [37], [38]. In [39]–[41], it is shown that the regularization parameter ε affects the quality of a solution to the general l_1-norm minimization problem $\min \|x\|_1 + 1/2\varepsilon \|y - Ax\|_2^2$. The best practice of finding a regularization value ε that produces a suboptimal solution (8) is to find it empirically for each specific case. For example, in [39], the regularization parameter was chosen as $\|2A^T x\|_\infty$. Likewise, in [40], the regularization parameter was chosen as $2\sigma\sqrt{\log n}$. Similarly, Park and Lee [41] set the regularization parameter as $2\sigma\sqrt{\log n}$ or 10^{-4}. We have chosen ε according to [40] and [41]. Throughout this study, the regularization parameter ε is set to $\varepsilon = 3 \times 10^{-3}$, which is shown to be efficient in terms of image quality.

In a single pulse-echo transmission, we use $N_{\text{Rx}} = 128$ array elements to record raw echo signals. Thus, we solve 128 equations independently, one for each receiving element in the array, as follows:

$$\begin{aligned} \mathbf{p}_1 &= \mathbf{G}_1 \mathbf{f}_1 \\ \mathbf{p}_2 &= \mathbf{G}_2 \mathbf{f}_2 \\ &\vdots \\ \mathbf{p}_{128} &= \mathbf{G}_{128} \mathbf{f}_{128}. \end{aligned} \tag{9}$$

Here, the ultrasound echo signals $\mathbf{p}_i$ and the transmission matrix $\mathbf{G}_i$ depend on the position of the corresponding receiving element i. The object image $\mathbf{f}_i$ itself shall remain the same throughout each receiving element $i \in \{1, 2, \ldots, N_{\text{Rx}}\}$. Thus, we can obtain a high-resolution compound image $\mathbf{f}_{\text{compound}}$ by summing together all reconstructed images $\hat{\mathbf{f}}_i$ and dividing by a total number of images as follows:

$$\mathbf{f}_{\text{compound}} = \left(\sum_{i=1}^{N_{\text{Rx}}} \hat{\mathbf{f}}_i \right) / N_{\text{Rx}} \tag{10}$$

where $\sum$ is a sum of all reconstructed images for each receiving element $i \in \{1, 2, \ldots, N_{\text{Rx}}\}$. In Section III-B, we further discuss how the number of reconstructed images $\mathbf{f}_i$ affects the quality of the final compound image $\mathbf{f}_{\text{compound}}$.

The optimization problem (8) can best recover the object image $\mathbf{f}_i$ when the mutual coherence μ among the columns of matrix $\mathbf{G}_i$ is low. For example, we define the mutual coherence μ of the spatial responses of two points separated by the distance d as follows:

$$\mu(d) := \max_{\substack{k \ne l \\ k,l \in \{1,\ldots,N_{\text{Sc}}\}}} \frac{|\langle \mathbf{g}_k, \mathbf{g}_l \rangle|}{\|\mathbf{g}_k\|_2 \|\mathbf{g}_l\|_2} \tag{11}$$

where $\mathbf{g}_k$ is the spatial response of the respective point scatterer at $\mathbf{r}_k$ position, $\mathbf{g}_l$ is the spatial response of point scatterer at $\mathbf{r}_l$ position, and $\langle \cdot, \cdot \rangle$ denotes the inner product. Note that the spatial responses are the result of interference between transmitted excitation signals. If we define the distance d between virtual points as a very small value, then the difference in the path traveled by the transmitted signals would be insignificant; this will yield spatial points with highly coherent spatial responses. In Section II-C, we explain how the

proposed random excitation signals $w_j(t)$ affect the coherence of the matrix $\mathbf{G}_i$. In Section II-D, we explain the relationship between the proposed excitation signals, the level of coherence of matrix $\mathbf{G}_i$, and the best achievable resolution.

C. Random Excitation Signals

We propose using excitation signals coded with random sequences to make spatial responses of individual point scatterers to be mutually incoherent. In such a case, the proposed method can reconstruct high-resolution ultrasound images as described in Section II-B. The following steps are used to generate the jth excitation signal for each $j \in \{1, 2, \ldots, N_{\mathrm{Tx}}\}$:

1) Generate a binary pseudorandom sequence $\mathbf{w}_j = [w_{j,1}\ w_{j,2}\ \cdots\ w_{j,N_w}]$ of length N_w where each element $w_{j,n}$, i.e., $n \in \{1, 2, \ldots, N_w\}$, is drawn from the binary set $\{-1, 1\}$ following the uniform distribution.
2) Convolve every element of the sequence $\mathbf{w}_j$ with the base signal of a half-cycle sine wave at the nominal frequency of f_c.
3) Repeat steps 1) and 2) for each jth element in the array.

We can now define the proposed excitation signals $w_j(t)$, coded with random sequences $\mathbf{w}_j$, in (3) as follows:

$$w_j(t) = \sum_{n=1}^{N_w} w_{j,n} u(t - T(2n-1)/2) \tag{12}$$

where $u(t) := A\cos(2\pi f_c t)\Pi(t/T)$ is the half-cycle base signal; $\Pi(t/T)$ is the rectangular signal which is equal to 1 inside the interval $[-T/2, T/2]$ and 0 otherwise; $2T = 1/f_c$ is the period of the base signal; A is the amplitude. Ideally, we want excitation signals to be completely random which would make spatial responses even more incoherent; however, a rapid oscillation of excitation signals can potentially be damaging to the piezo-electric crystals. Therefore, we smoothed the sequences $\mathbf{w}_j$ using a sine wave as given in (12). The duration of excitation signals can be controlled by either changing the frequency f_c of the sine wave or the length N_w of the binary random sequences $\mathbf{w}_j$.

In this study, we produce excitation signals with binary sequences of the length $N_w = 13$ and the nominal frequency $f_c = 3$ MHz. This gives excitation signals with 4.5-μs duration. For example, we set the random sequences $\mathbf{w}_j$ for $j = 1, 2$ as follows:

$\mathbf{w}_1 = (-1, -1, -1, -1, 1, 1, -1,\ 1, -1, -1, 1, -1, 1)$ and
$\mathbf{w}_2 = (-1, -1, -1, -1, 1, -1, 1,\ 1, 1, -1, 1, 1, 1)$.

Then, the corresponding random excitation signals are shown in Fig. 3(a) and (b). Let us consider two spatial points described by a vector $\mathbf{r}_k = (x, y, z)$ for $k = 1, 2$ with the coordinates $\mathbf{r}_{k=1} = (0.25, 0, 50)$ mm and $\mathbf{r}_{k=2} = (-0.25, 0, 50)$ mm. When we transmit random excitation signals $w_j(t)$ from two array elements, the spatial response of the scatterer at $\mathbf{r}_{k=1}$ is shown in blue in Fig. 3(c). The spatial response of the scatterer at $\mathbf{r}_{k=2}$ is shown in red in Fig. 3(c). The shapes of the spatial responses are a direct result of the constructive and destructive interference that occurs between the transmitted random excitation signals.

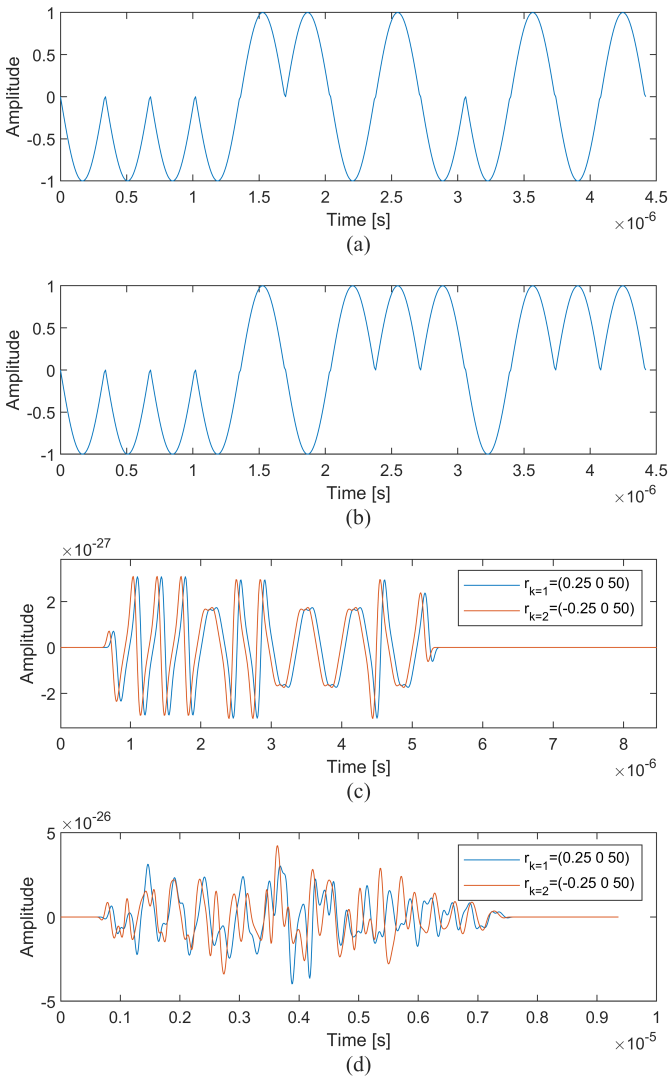

Fig. 3. Examples of random excitation signals. (a) Random excitation signal w_1(t). (b) Random excitation signal w_2(t). Simulated ultrasound signals of point scatterers with lateral separation of 0.5 mm, (c) when only two array elements transmitted random signals and (d) when all 128 array elements transmitted random signals.

By increasing the number of transmitted random signals $w_j(t)$ for $j \in \{1, 2, \ldots, N_{\mathrm{Tx}}\}$, we can further reduce the correlation between two different adjacent spatial points. With (11), the coherence μ between any two column vectors $\mathbf{g}_k$ and $\mathbf{g}_l$ can be measured. Similarly, we measure the coherence of a random excitation signal $w_1(t)$ and $w_2(t-\tau)$, a delayed random excitation signal $w_2(t)$, that is

$$\langle w_1(t), w_2(t-\tau)\rangle = \frac{\int_0^{N_w T+\tau} w_1(t) w_2(t-\tau) dt}{\int w_1(t)^2 dt \int w_2(t)^2 dt} \tag{13}$$

where $N_w T$ is the duration of each excitation signal $w_j(t)$, and τ is the difference between the arrival time of signal $w_1(t)$ and that of $w_2(t)$ at the observation point $\mathbf{r}_k$. The arrival time-delay τ shall depend upon the difference of total distance the wave has traveled. Thus, delay τ depends on the spacing $\|\mathbf{r}_1 - \mathbf{r}_2\|$ between the transducer elements. When the more number of array elements are used to

transmit the proposed random signals, the more random the interference pattern becomes, and the more incoherent the spatial responses of the relevant point scatterers become. For example, we let $N_{\mathrm{Tx}} = 128$, and use all 128 elements to emit random signals $w_j(t)$ for all $j \in \{1, 2, \ldots, N_{\mathrm{Tx}}\}$. Then, the spatial response of the scatterer at $\mathbf{r}_{k=1}$ is shown in Fig. 3(d) in blue. The spatial response of the scatterer at $\mathbf{r}_{k=2}$ is shown in red. In this particular case, the mutual coherence (11) of the two impulse responses equals 0.04.

D. Theoretical Resolution Limit

Conventional ultrasound systems which use delay-and-sum beamforming are diffraction-limited systems. The diffraction resolution limit is $\lambda/2$ [2]. According to [3], the best lateral resolution of conventional ultrasound systems is one wavelength λ of the transmit pulse. For typical frequencies in the range of 3–15 MHz, the lateral resolution corresponds to 0.5–0.1 mm. The best axial resolution is two wavelengths 2λ [3]. For typical frequencies in the range of 3–15 MHz, the axial resolution corresponds to 1.0 to 0.2 mm.

In our approach, the resolution limit is the grid size d, a real-valued scalar. We aim to minimize d while having the maximum correlation μ remain to be small. If the grid size d is set too small, the coherence μ of a transmission matrix will be high, thus making it difficult to reconstruct the image $\hat{\mathbf{f}}_i$. Given a set of excitation signals $\{w_j(t) : j = 1, 2, \ldots, N_{\mathrm{Tx}}\}$ and a receiver element $i \in \{1, 2, \ldots, N_{\mathrm{Rx}}\}$, we can obtain the transmission matrix $\mathbf{G}_i$ and find the smallest distance d subject to sufficiently small mutual coherence μ of $\mathbf{G}_i$, that is, $\mu < \delta$. Thus, the resolution limit of the proposed method is closely related to the optimization problem (8). The maximum achievable resolution $\hat{d}$ is then formally given in terms of the mutual coherence (11) of the matrix $\mathbf{G}_i$ as follows:

$$\hat{d} := \min_d \ \mu(d) \quad \text{s.t. } \mu < \delta \tag{14}$$

where $\delta > 0$ is a utility parameter of a positive real number. For example, when the distance d between two point scatterers decreases, the value of the coherence μ will naturally increase (11) because the phase shift between the transmitted random signals at two spatial points will become less and less noticeable. The theoretical resolution of the proposed method is not limited by the diffraction, but rather by the coherence of the matrix $\mathbf{G}_i$. The coherence of the transmission matrix describes the correlation between spatial responses of point scatterers. Therefore, we identify the tradeoffs that exist between the achievable image resolution (the distance d separating the scatterers on the virtual grid) and the coherence of the matrix $\mathbf{G}_i$.

In Section II-C, we have discussed that a more complex wavefront of random interference can be used to reduce the coherence of a transmission matrix and thus improve image resolution. Likewise, the coherence of the matrix $\mathbf{G}_i$ depends on the nominal frequency and length of pseudorandom sequences. It would be too difficult to obtain the optimal solution based on all possible combinatorial variations of these parameters. We now want to discuss how we have found the excitation signal set $\{w_j(t) : j = 1, 2, \ldots, N_{\mathrm{Tx}}\}$ and maximum resolution $\hat{d}$. To diminish the complexity, we have devised a reduced complexity setting. Under this setting, calculation of the mutual coherence is done only for a reference set of the lateral point scatterers. Over this reference set, the optimization in (14) is performed for a certain selected δ. We refer to this as μ_L the local coherence. There are several reference sets we have tried. We let $\delta = 0.35$ and aim to find the minimum grid size. The optimal reference set is the lateral point scatterers which are separated by 0.25 mm and located at a depth of 50 mm. On this set of lateral points, the proposed set of excitation signals, the proposed nominal frequency, and the length of the pseudorandom sequence have been found. They are the nominal frequency of $f_c = 3$ MHz and the length of the pseudorandom sequence of $N_w = 13$. We further discuss how these parameters are related with each other. We let the speed of sound $c_0 = 1540$ m/s and the sampling frequency $f_s = 40$ Msamples/s. The grid size of $d = 0.25$ mm is obtained from μ_L for $\delta = 0.35$. The local mutual coherence is $\mu_L = 0.3$ and the mutual coherence is $\mu = 0.79$. Any excitation signals generated with the same parameters would produce the desired effect of random interference and can be used to reconstruct high-resolution images.

E. Transmission Matrices for Experimental Study

In this section, we provide a description of procedures to generate transmission matrices $\mathbf{G}_i$ used in the real phantom experiments. The direct method obtaining spatial responses for experimental study would be using a hydrophone with a translation stage. However, it is a time-consuming and error-prone method because a hydrophone has to be perfectly aligned with a large number of different spatial points. Therefore, we propose an alternative method of obtaining spatial responses. We first measure the echo signals of the random excitation signals reflected from a plastic plane in a simple water tank experiment setup. Then, we generate approximations of spatial responses as the sum of delayed versions of measured random signals. Next, we describe a step by step procedures used to obtain transmission matrices $\mathbf{G}_i$s for $i \in \{1, 2, \ldots, N_{\mathrm{Rx}}\}$.

First, the linear transducer array was aligned perpendicular to the plastic plane, which was placed at 4 cm depth in a water tank. We assigned random excitation signals (12) to all array elements. Next, in a series of pulse-echo transmissions, we activated one by one each transmitting element and measured the ultrasound wavefront reflected from the plastic plane. We used the same transducer array to record the reflection of the plastic plane echo signals. Let $\mathbf{A}$ be an $M \times N_{\mathrm{Tx}} \times N_{\mathrm{Rx}}$ 3-D real-valued matrix where M is the total number of signal samples, N_{Tx} is the number of transmitting elements, and N_{Rx} is the number of receiving elements. $\mathbf{A}[\mathrm{s}, j, i]$ denotes the (s, j, i) component of an array $\mathbf{A}$ for each $\mathrm{s} \in \{1, 2, \ldots, M\}$, $j \in \{1, 2, \ldots, N_{\mathrm{Tx}}\}$, and $i \in \{1, 2, \ldots, N_{\mathrm{Rx}}\}$. Fixing one variable, i.e., $\mathbf{A}[M, j = 1, N_{\mathrm{Rx}}]$ notation, is to mean a 2-D matrix of the matrix $\mathbf{A}$.

In Fig. 4, we show the echo signals acquired when only $j = 1$ element emitted a random signal $w_1(t)$. The echo signals were normalized and aligned by applying time-delays. We arranged the measured echo signals into a 3-D matrix $\mathbf{A}$.

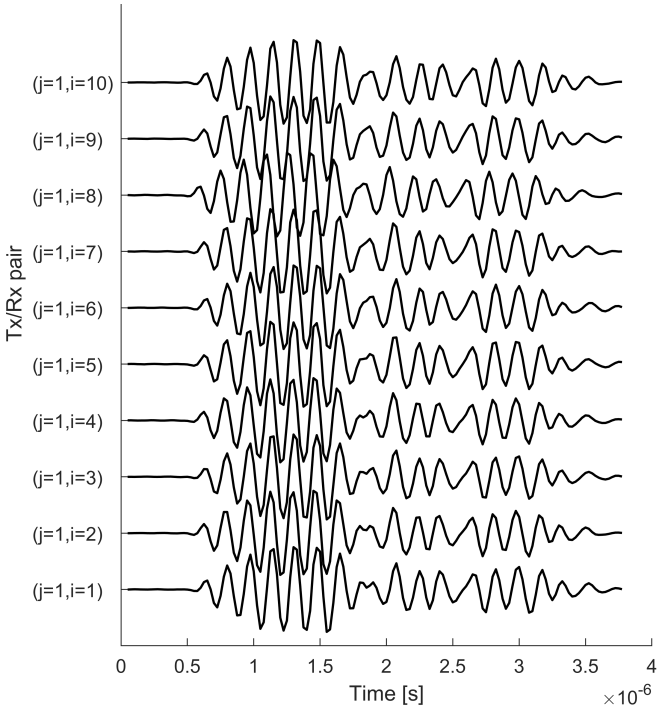

Fig. 4. Echo signals of the proposed excitation signals measured in the water tank experiment for the corresponding pair of transducer elements (j,i). Only the first $j = 1$ transmitting element were activated; all N_{Rx} receiving elements were used to receive the echo signals. The first ten echo signals are shown.

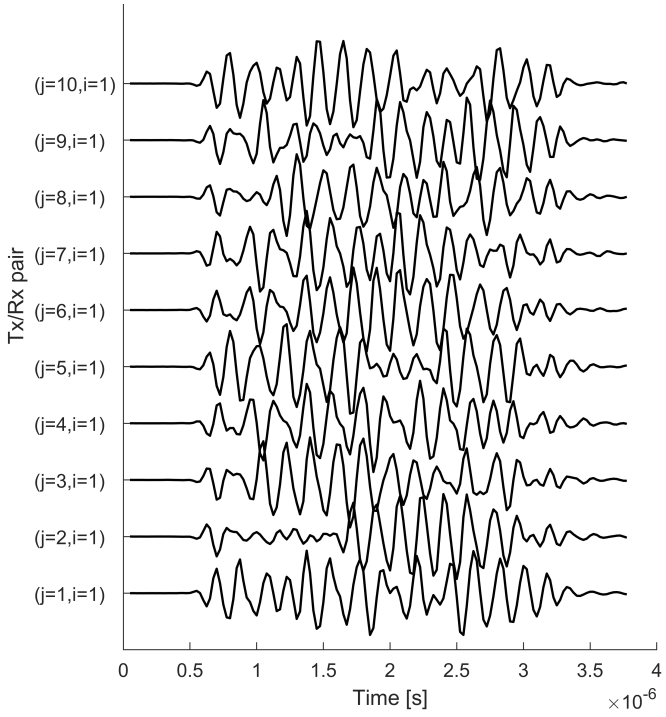

Fig. 5. Echo signals of the proposed excitation signals measured in the water tank experiment for the corresponding pair of transducer elements (j,i). Each transmitting element j was assigned with a unique random excitation signal. The transmitting elements were activated one by one. The receiving element $i = 1$ is used to record echo signals. The first ten echo signals are shown.

Then, $\mathbf{A}[M, j = 1, N_{\mathrm{Rx}}]$ corresponds to a 2-D matrix M by N_{Rx} with each column representing an echo signal as shown in Fig. 4. These echo signals exhibited a very small variation and that the shape of the reflected echo signals was identical. We measured echo signals individually for every pair of transmitting and receiving elements. The echo signals of the matrix $\mathbf{A}[M, j = 1, N_{\mathrm{Rx}}]$ are shown in Fig. 4. Similarly, $\mathbf{A}[M, j = 2, N_{\mathrm{Rx}}]$ would represent echo signals acquired using all $N_{\mathrm{Rx}} = 128$ receiving elements when only the second $j = 2$ element transmits the random excitation signal $w_2(t)$. Likewise, Fig. 5 shows the matrix $\mathbf{A}[M, N_{\mathrm{Tx}}, i = 1]$ that corresponds to the echo signals acquired using the receiving element $i = 1$ when all $j \in \{1, 2, \ldots, N_{\mathrm{Tx}}\}$ elements individually transmit a corresponding random signal $w_j(t)$.

Let $\mathbf{B}$ be an $N_{\mathrm{Tx}} \times N_{\mathrm{Sc}}$ 2-D real-valued matrix. $\mathbf{B}[j,k]$ denotes the (j,k) component of $\mathbf{B}$ for each $j \in \{1, 2, \ldots, N_{\mathrm{Tx}}\}$ and $k \in \{1, 2, \ldots, N_{\mathrm{Sc}}\}$. Next, we define ROI as a 2-D virtual grid, shown in Fig. 2. We use $\|\mathbf{r}_j - \mathbf{r}_k\|$ to find the distance information from every array element to every spatial point on the virtual grid. We arrange distance information into the matrix $\mathbf{B}$. Using the matrix $\mathbf{B}$, we can calculate the time required for a transmitted random signal to travel to the spatial point and return to the receiving element. Then, we can find the spatial impulse response of the spatial point at $\mathbf{r}_k$ by applying corresponding time-delay from the matrix $\mathbf{B}$ to the measured echo signals in the matrix $\mathbf{A}$; the delayed echo signals of corresponding random excitation signals are shown in Fig. 6. Then, the spatial impulse response $\mathbf{g}_k$ is found by summing and normalizing the delayed versions of measured random excitation signals. We repeat this procedure for every spatial point k in the ROI. We use the procedure described above to generate the matrix $\mathbf{G}_i$ for our real phantom experiment.

One may wonder if the delay-and-sum concept used to generate the proposed transmission matrices were affected by the diffraction. However, we used the delay-and-sum concept only to generate spatial responses from measurements of random excitation signals. The excitation signals are measured in the water tank experiment; thus, the impact of secondary reflections caused by the acoustic diffraction effect is negligible.

In summary, we share different approaches used to generate transmission matrices for our experimental study. In the beginning, we have attempted to reconstruct an image of the real phantom using transmission matrices from the simulation study. However, the limited bandwidth of the transducer means that the simulated spatial responses do not accurately represent the actual spatial responses in the real experiment [42]. Thus, the resulting reconstructed images have suffered from low resolution. Also, we considered using a wire and a point target instead of a plastic plane. However, it was difficult to measure the responses of the excitation signals throughout the whole experiment. Since the target object is small, it reflected a weak noisy signal. To obtain consistent measurements, in addition, a smaller target has to be much more precisely aligned with the transmitting array element. A high precision alignment was difficult to be achieved in our experimental setup because transducer elements are separated by a very small distance of 0.03 mm and embedded in a closed housing.

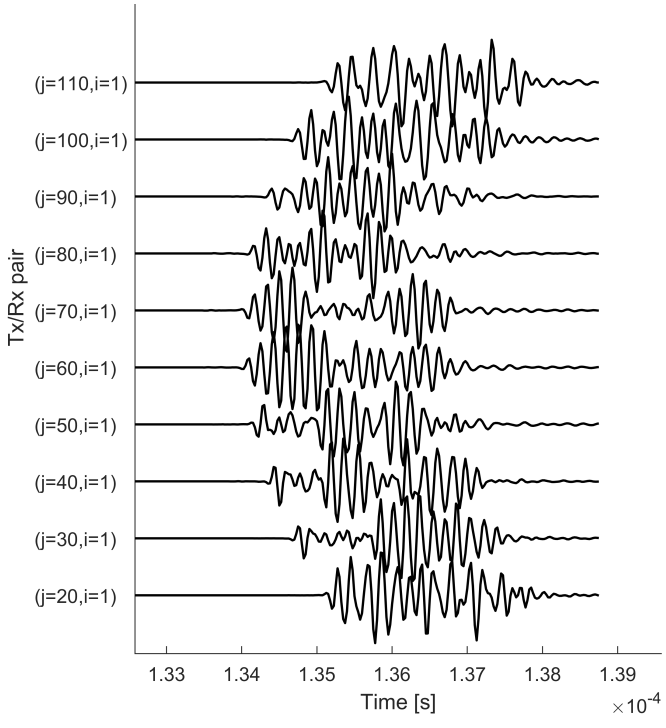

Fig. 6. The delayed echo signals of the proposed excitation signals measured in the water tank experiment for the corresponding pair of transducer elements (j,i) and the spatial point at $\mathbf{r}_k$.

III. Results

In this section, we present simulation and experimental results; we use several phantoms to verify the proposed method. The proposed method shows much better image resolution when compared with the conventional methods that use delay-and-sum beamforming techniques. In the simulation, we have achieved a 0.25-mm resolution on nonsparse objects. In the experiment, we demonstrate successfully reconstructed images of a tissue-mimicking phantom.

A. Simulation Study

The simulation was performed using Field II ultrasound software [35], [36]. A linear transducer with 128 elements was simulated where each array element was excited with a random signal as described in Section II. In the simulation, we defined a transducer array similar to the transducer array that was available for the experimental study. The elements of the transducer array were 4.5 mm high and 0.3 mm wide, and they were separated by 0.03-mm gaps. The central frequency and sampling frequency were set to 3 and 40 MHz, respectively. The ROI was set from 35 to 55 mm in the axial direction and from -10 to 10 mm in the lateral direction. Synthetic phantoms were defined on a virtual grid with a resolution of $d = 0.25$ mm. This gave us a square image with 81 points in the axial/lateral directions and $N_{\text{Sc}} = 6561$ point scatterers. The speed of sound is again set to $c_0 = 1540$ m/s. The density of the phantom is set to $D = 1000\ \text{kg/m}^3$. The acoustic impedance is equal to $Z = 1.54 \times 10^6 \text{kg}/(\text{m}^2 \cdot \text{s})$. The frequency-dependent attenuation around 3 MHz is 0.5 dB/(MHz $\cdot$ cm). The simulation study was performed using a small ROI due to the extensive time required to generate transmission matrices.

First, we simulate a synthetic phantom with two closely placed point targets as shown in Fig. 7. Two-point scatterers are placed at a depth of 45 mm with 0.25-mm separation in the lateral direction. The scatterer map is as shown in Fig. 7(a). We show a side-by-side comparison of the images obtained using the conventional focused B-mode method and the proposed interference-based method. Fig. 7(b) shows the image obtained using the focused method. The image was reconstructed using 128 scanlines with the focal point set to 45 mm in the axial direction. With the B-mode method, two-point targets appear with sidelobes and cannot be resolved from each other. However, with the proposed method, we can reconstruct the image of the two points as shown in Fig. 7(c). The location and intensity of reconstructed scatterers precisely match the scatterer map. Moreover, the radio frequency (RF) signal acquired at a single channel (in blue) and a signal reconstructed using the proposed method (in red) perfectly match as shown in Fig. 7(d). The RF signal is a superposition of the impulse responses of the two point scatterers. Therefore, a correct combination of impulse responses, which corresponds to our targets, has been found. In Fig. 7(e), we plot the intensity profiles taken at the 45-mm position of the scatterer map (blue), its B-mode image (yellow), and the image reconstructed using the proposed method (red). Fig. 7(e) shows that the proposed method can recover the exact position and amplitude of the point scatterers, whereas the scatterers are not distinguishable in the conventional B-mode method.

In Fig. 8, a Shepp–Logan phantom is used to evaluate the reconstruction performance of the proposed method on nonsparse objects. The phantom consists of a large number of scatterers of varying intensities, as shown in Fig. 8(a). The image obtained with the conventional focused B-mode method is shown in Fig. 8(b). The image is blurred; in particular, the details inside the circle are not visible. In the proposed interference-based method, the image contains accurate details of the phantom structures where the phantom boundaries and inner circles are clearly identifiable, as shown in Fig. 8(c). Moreover, the contrast in the image is much closer to that of the original phantom image. To demonstrate the proposed method's accuracy, we plotted the intensity profiles of the Shepp–Logan phantom at 45 mm depth, as shown in Fig. 9. The intensity profiles for the scatterer map, the focused B-mode method, and the interference-based method are shown in blue, yellow, and red, respectively. In Fig. 9, we can observe that the focused B-mode fails to provide details for the phantom's boundaries. Due to the sidelobes, the intensity profile of the scatterers inside the phantom does not match that of the scatterer map. In Fig. 9, the proposed method can reconstruct the phantom image with high accuracy. The image of the proposed method in Fig. 8(c) shows that the overall details and contrast are much better than the image obtained using the conventional beamforming-based methods.

B. Configuration of the Receiving Array

Using a single transmission of the proposed wavefront of random interference, we can reconstruct up to 128 images $\hat{\mathbf{f}}_i$, one for each receiving element $i \in \{1, 2, \ldots, N_{\text{Rx}}\}$. To achieve

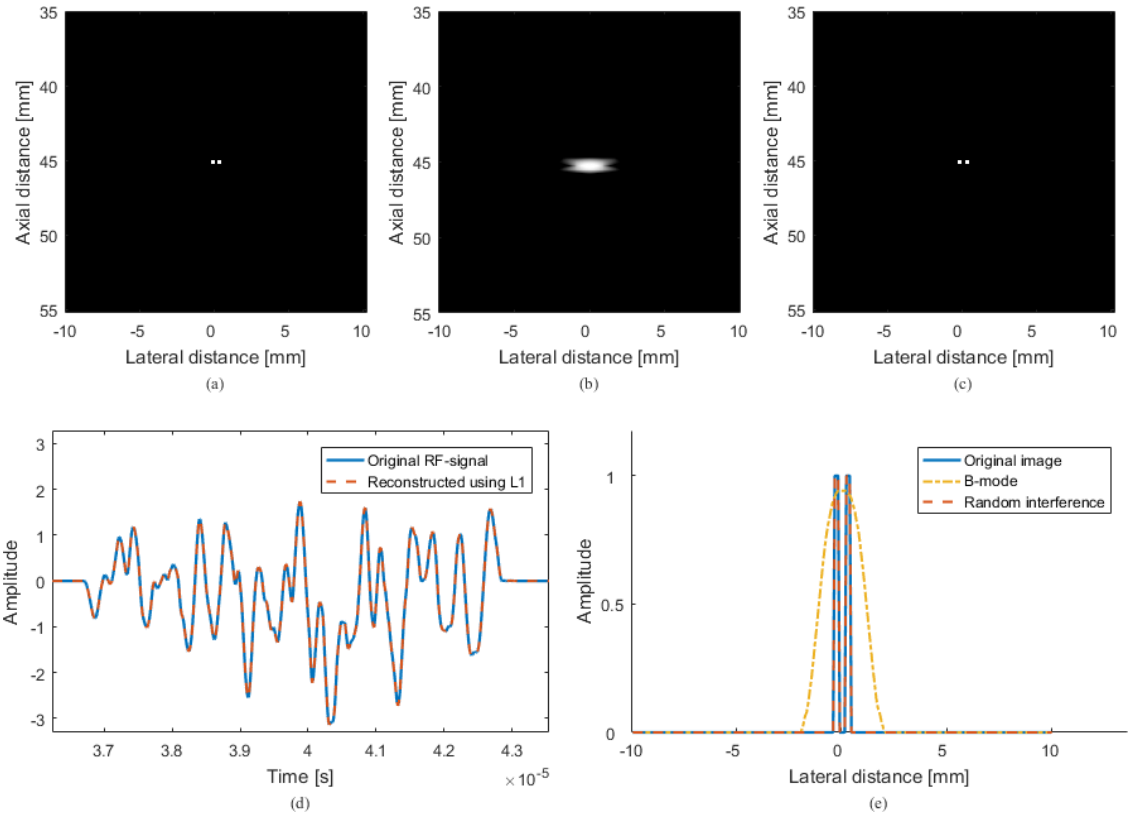

Fig. 7. Simulation study using a two-point phantom. The phantom features two point targets that are 45 mm from the transducer array with a 0.25-mm separation in the lateral direction between the targets. (a) Image of the scatterer map. (b) Image of the focused B-mode method. (c) Image of the proposed method. (d) Ultrasound signal acquired at the single receiving channel is plotted in blue; this signal consists of the superposition of impulse responses that correspond to two point targets. The red plot is the reconstructed signal using the interference-based method. (e) Plot of the intensity profiles of the original image, focused B-mode image, and the image obtained using the proposed method. Images are shown with a 60-dB dynamic range.

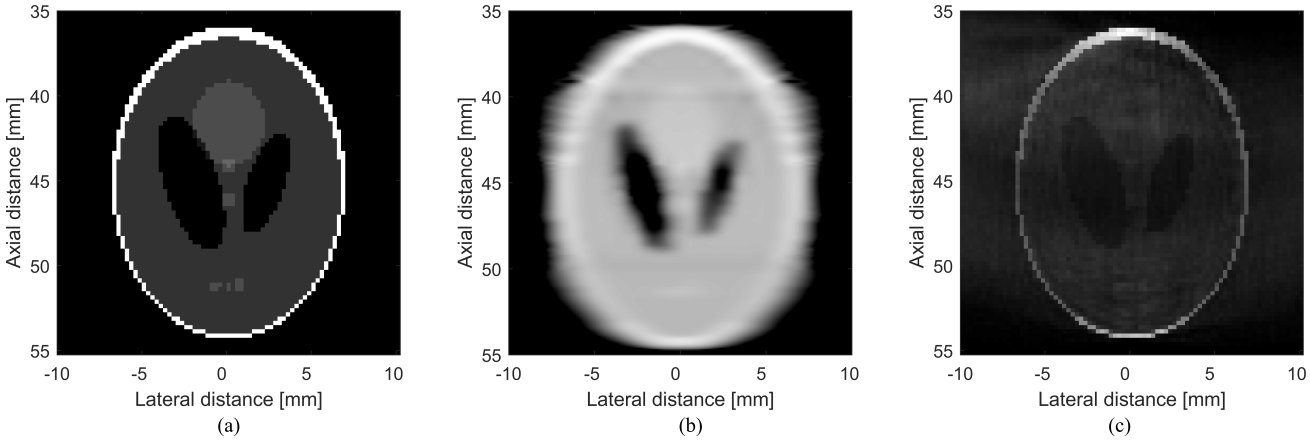

Fig. 8. Simulation study using the Shepp–Logan phantom. (a) Original phantom image. (b) Reconstruction using the focused B-mode method. (c) Reconstruction using the interference-based method. Images are shown with a 60-dB dynamic range.

high spatial resolution, we compound together all 128 images $\hat{\mathbf{f}}_i$ as given in (10). In addition to the resolution improvements, we are interested in evaluating the dependence of the image quality given a different number of compounding images. The results are shown in Fig. 10. We consider seven different configurations for the receiving array; Table I summarizes the details of proposed array configurations including information about the total number of active elements in the receiving array, mean squared error (MSE), peak signal-to-noise ratio (PSNR), and SNR. The results of MSE, PSNR, and SNR are given with respect to the original Shepp–Logan phantom shown in Fig. 10(a). For example, the image shown in Fig. 10(b) was compounded using 128 images. The image provides clear details of the synthetic phantom. The image shown in Fig. 10(g) was reconstructed using only 15 receiving array elements. Table I shows that MSE becomes smaller

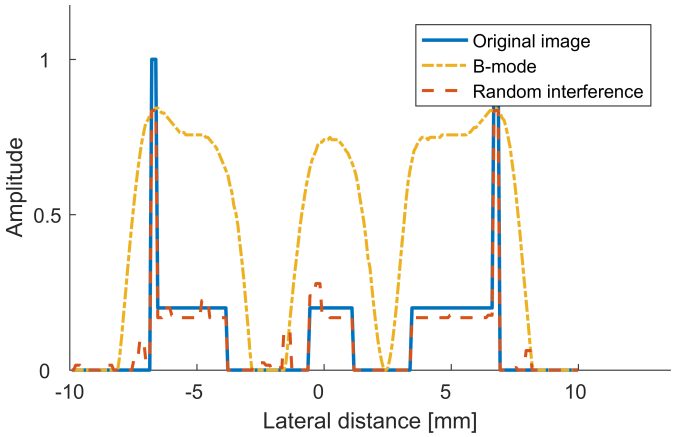

Fig. 9. Intensity profiles from the Shepp–Logan phantom study. Image intensity profiles are taken at 45 mm in the axial direction. Blue color indicates intensity profile of the original scatterer map. Orange indicates intensity profile of focused B-mode, and red indicates intensity profile of interference-based method.

TABLE I
DEPENDENCY OF IMAGE QUALITY ON THE NUMBER OF ARRAY ELEMENTS

	Name	Total number of elements	MSE	PSNR [dB]	SNR [dB]
(a)	Original phantom image	~	~	~	~
(b)	All elements of the array	128	0.0158	17.99	5.60
(c)	Every 3rd element	43	0.0162	17.90	5.51
(d)	Every 5th element	26	0.0164	17.86	5.47
(e)	Elements in the interval [30,98]	69	0.0120	19.21	6.81
(f)	Elements in the interval [40,88]	49	0.0119	19.23	6.84
(g)	Every 2nd element in the interval [50,78]	15	0.0122	19.20	6.80
(h)	Single element	1	0.0255	15.93	3.54

when a subset of elements in the middle of the array is used. According to the MSE, we conclude that fewer receiving elements are sufficient to achieve image resolution similar to Fig. 10(b). This phenomenon can be explained by the acceptance angle of the array elements. The effect of random interference depends on the number of interfering waves. Thus, the random interference is stronger in the center of the ROI. As a result, we observe fewer errors when reconstructing images using RF-data from elements in the middle of the array. Similarly, the PSNR and SNR improve as we increased the number of reconstructed images used to obtain a compound image (10) (see Table I). In addition, we would like to

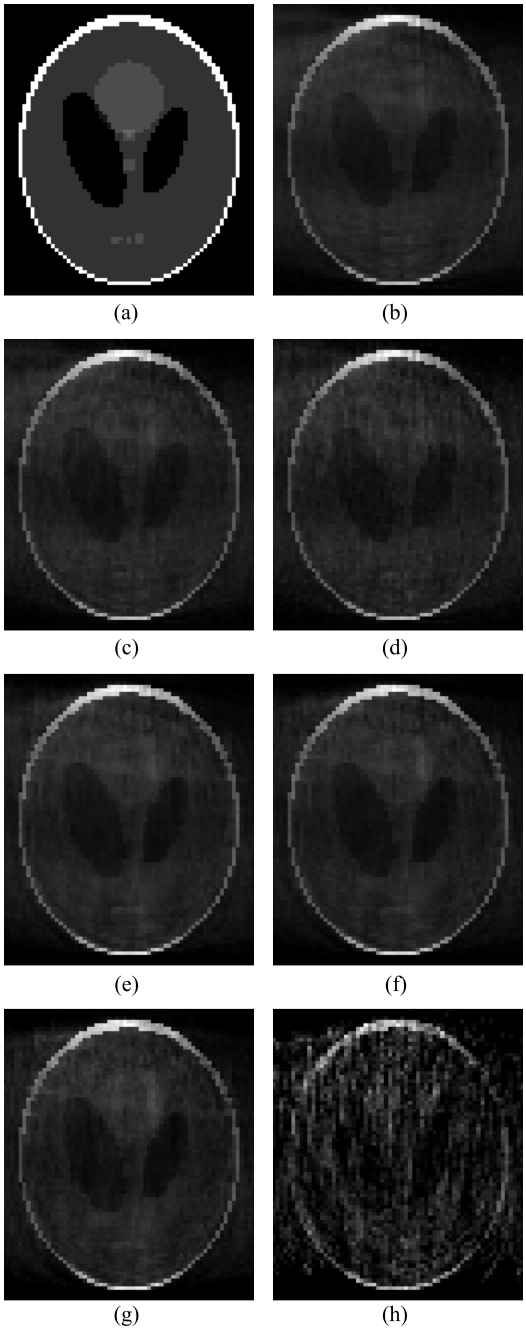

Fig. 10. Simulation study on dependence of image quality on the number of receiving elements. (a) Original image of the Shepp–Logan phantom. (b)–(h) Corresponding ultrasound images when different numbers of receiving elements are used. The details of different array configurations are given in Table I. Images are shown with 60-dB dynamic range.

emphasize that in the simulation study, the proposed method can reconstruct a 2-D image from a single receiving element, and the image is shown in Fig. 10(h). The image is corrupted by noise artifacts; however, strong reflecting points such as the boundaries of the phantom have been reconstructed correctly.

C. Experimental Setup

To verify our proposed method, we developed a research ultrasound system capable of generating the proposed

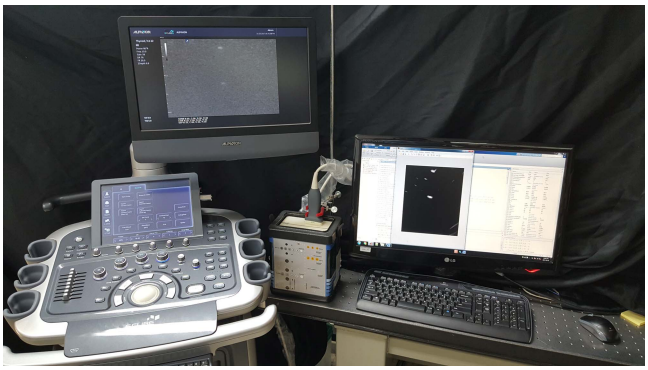

Fig. 11. Image of the experimental setup. Ultrasound research equipment with 128-element linear transducer, synthetic phantom, and second monitor to display the reconstructed image using the proposed method.

ultrasound wavefront of random interference. A photograph of the experimental setup is shown in Fig. 11. The ultrasound system is a COSMOS research unit developed in collaboration with Alpinion medical systems. The system features a linear transducer array with 128 piezo-electric elements and a central frequency of 3–12 MHz. The array elements are 4.5 mm high and 0.3 mm wide, and the elements are evenly separated from each other with a 0.03-mm gap. The sampling frequency is set to 40 MHz and the frequency of the transmitted ultrasound wave is 3 MHz. All parameters in the experimental study were set to reproduce our simulation protocol. The system is equipped with an arbitrary wave generator (AWG) to enable the transmission of random signals. The AWG has a dedicated memory that is used to store random excitation signals for every transmitting channel. The memory can store an array of size 128×2048 of eight-bit data where each row is assigned to the corresponding transmitting element of the transducer array.

In this experiment, we use a commercially available phantom CIRS Model 040GSE. The phantom is made of a solid elastic hydrogel that mimics the properties of human tissue. To demonstrate differences between the conventional beamforming-based method and the proposed interference-based method, we first provide a side-by-side comparison of RF-data (see Fig. 12). The transducer array was aligned such that the 64th element of the array was perpendicular to the vertical distance group consisting of nylon wires. All elements of the transducer array are simultaneously excited with the proposed random excitation signals which yield an incident wavefront of random interference. The echo signals are shown in Fig. 12(a). In Fig. 12(b), we provided a side-by-side comparison of echo signals acquired at 64th array element using the conventional beamforming-based method and the proposed interference-based method. Fig. 12 shows the fundamental differences between the two methods. The echo signal acquired using beamforming-based method is shown in black in Fig. 12(b). The signal features strong echoes reflected from the nylon wires at corresponding depths of 1, 2, 3, and 4 cm, respectively. The echo signal acquired using the proposed interference-based method is shown in blue in Fig. 12(b). Due to the use of the unfocused transmission of random excitation signals, the signal shown in blue in Fig. 12(b) features multiple reflections from different spatial directions. Note that in the case of the proposed method, the strength of the echo signals is comparable to the level of the strength of echo signals in the conventional beamforming-based method.

D. Experimental Study

To demonstrate that the proposed interference-based method improves spatial resolution, we have selected two regions of the phantom. The ROI spans 55 mm in the axial direction and 40 mm in the lateral direction. The resolution of the virtual grid was $d = 0.25$ mm. This gave us an image with $N_{\text{Sc}} = 38801$ point scatterers. In the simulation study, the images are reconstructed using RF-data from one pulse-echo transmission of random signals. In the experimental study, the images are reconstructed using RF-data acquired using ten pulse-echo transmissions due to strong acoustic noise and attenuation. In each pulse-echo transmission, we use a different set of randomly generated signals. In total, we reconstruct and compound together 1280 images. On a standard computer with Intel Core i7-6800K CPU and NVIDIA GTX 1060 GPU using a single thread, one image is reconstructed in approximately 4 s. The final compounded image is reconstructed in approximately 2 h. The RF-data were preprocessed using direct current (DC) cancelation and time gain compensation (TGC). The elements of the transducer array have acceptance angles, and not all spatial points contribute to the echo signal received by the ith transducer element. Therefore, in (7), we use a submatrix of $\mathbf{G}_i$ and subset of $\mathbf{f}_i$ that represent only point scatterers within the acceptance angle of the receiving element. For example, in Fig. 13, we show the acceptance angles for channel numbers 1, 64, and 96. The rest of the image reconstruction steps are the same as described in Section II-B.

The first region includes vertical/horizontal groups. The images of the first region are shown in Fig. 14. The ROI includes eight 0.1-mm-diameter nylon wires and a cyst. The nylon wires were separated by 10-mm gaps, with the first wire located at 10 mm depth from the transducer. In Fig. 14(a), we show an image reconstructed using the conventional focused B-mode method with 128 scanlines. In Fig. 14(b), we show an image reconstructed using the proposed interference-based method. The nylon wires in the case of the proposed method can be clearly observed without sidelobes. In addition, the level of speckle noise is significantly reduced in the proposed method. The image region with cyst target was also accurately reconstructed. The proposed interference-based method is a clear improvement over the conventional B-mode method.

The second region includes axial/lateral resolution groups (see Fig. 15). The group includes 12 0.08-mm-diameter nylon wires. The wires separated by 4, 3, 2, 1, 0.5, and 0.25 mm in the axial and the lateral directions. The image obtained using the conventional focused B-mode method with 128 scanlines is shown in Fig. 15(a). The ultrasound image reconstructed using the proposed interference-based method is shown in Fig. 15(b). A two time magnified images of axial/lateral resolution groups are shown in Fig. 15(c) and (d). Fig. 15

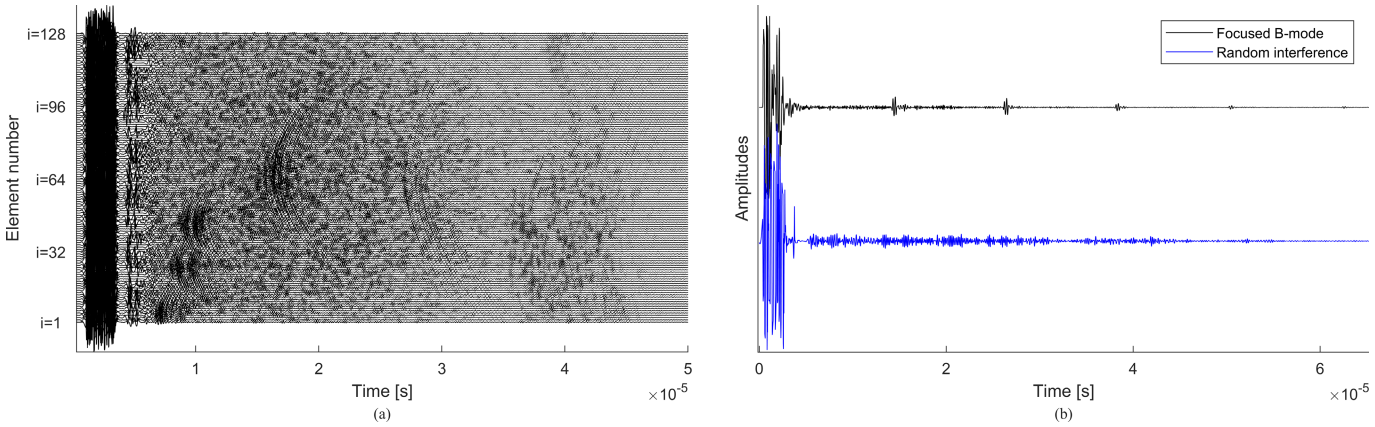

Fig. 12. Raw RF data acquired during a real phantom experiment. (a) Each line corresponds to a single RF signal acquired using one of the 128 array elements when all of the array's elements were simultaneously excited with the proposed random excitation signals. (b) Comparison of the RF signals acquired using 64th element of the array. The RF signal acquired using the conventional focused B-mode method is plotted in black; the sampled RF signal features strong reflections from nylon wires at 1, 2, 3, and 4 cm depths, respectively. The RF signal acquired at the 64th element of the array using the proposed interference-based method is plotted in blue; the sampled RF signal features strong echo reflections across all time samples.

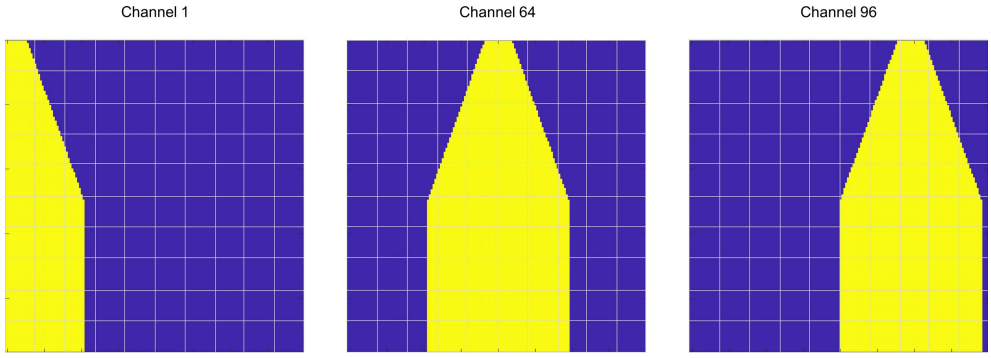

Fig. 13. Illustration of how a subset of spatial points is selected using acceptance angle of the array element.

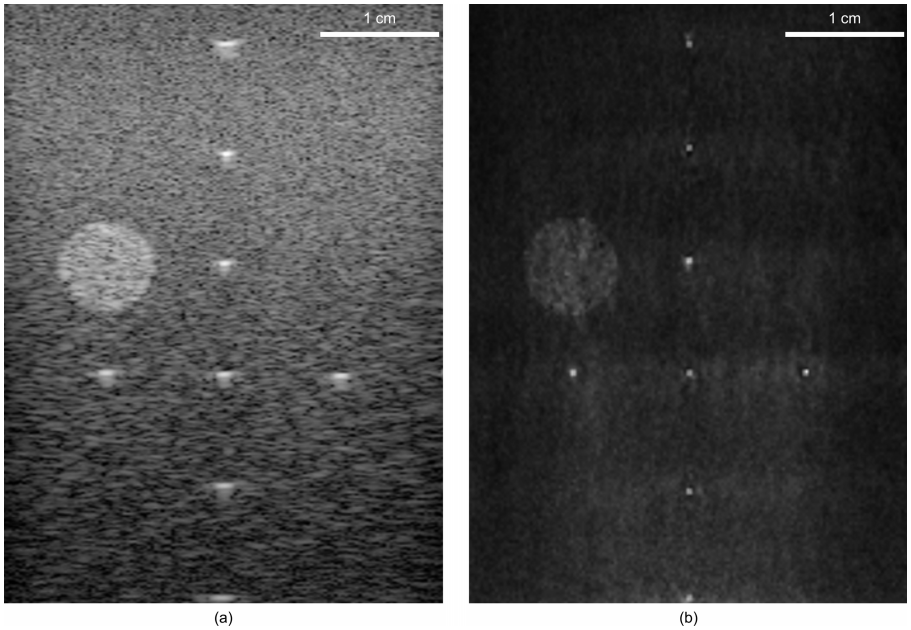

Fig. 14. Experimental study using synthetic silicon phantom CIRS 040GSE. A side-by-side comparison of the region with vertical/horizontal groups. (a) Image reconstructed using the conventional focused B-mode (delay-and-sum-beamforming) method. (b) Image reconstructed using the proposed interference-based method. Images are shown with 60-dB dynamic range.

shows that the proposed method provides much better details of nylon wires compared with the conventional method.

In the proposed interference-based method, the ultrasound images are reconstructed using *a priori* measurements

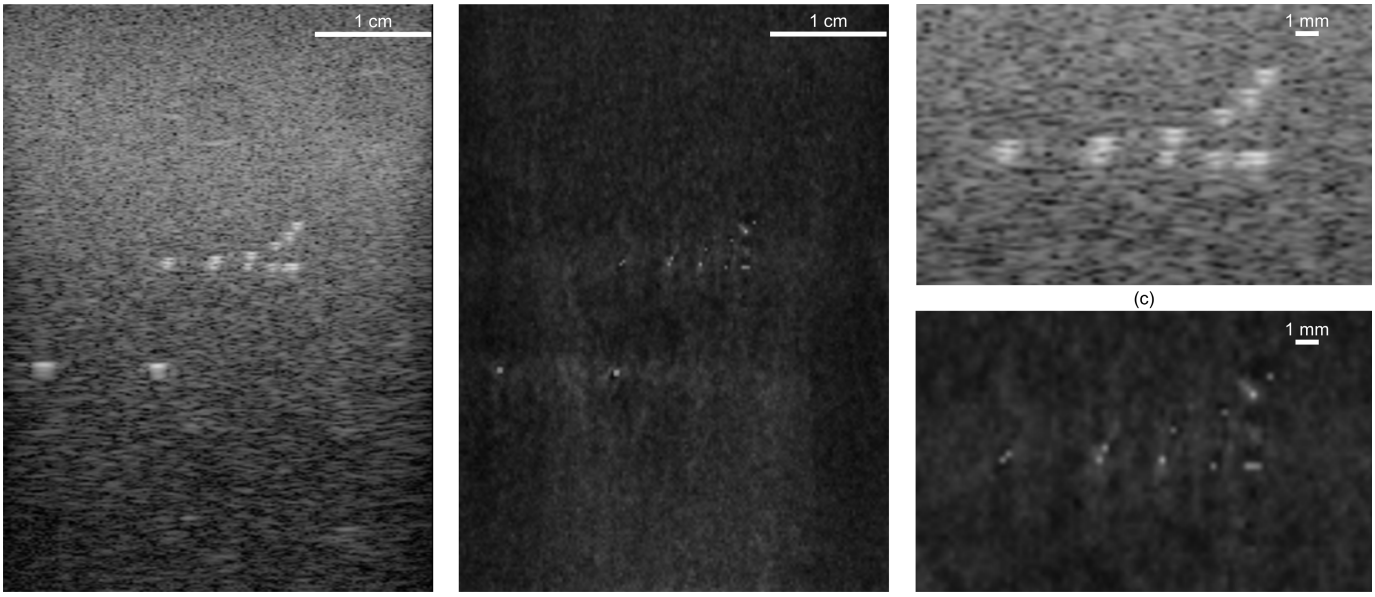

Fig. 15. Side-by-side comparison of the region with axial/lateral resolution groups. (a) Image reconstructed using the conventional focused B-mode method (delay-and-sum-beamforming). (b) Image reconstructed using the proposed interference-based method. (c) and (d) Two time magnified images of the conventional and proposed methods. All images are shown with 60-dB dynamic range.

TABLE II
COMPARISON OF DIFFERENT SONOGRAPHY METHODS

Parameters	The proposed interference-based method	N. Wagner [16] 2012	G. David [21] 2015	J. Liu [20] 2017	P. Kruisinga [30] 2017	G. T. Clement [25] 2005
Tx scheme	- 10 firings of unfocused random wavefront - Excitation random signals - 128 channels	- Focused transmission - 120 pulse–echo transmissions	- 1 plane-wave - 128-channels	- 32 firings of randomly apodized excitation - 128-channels	- Rotating single element with random mask - 72 Tx positions	- Single element (diameter=60)
Rx scheme	- 128 channels	- 64 channels	~	- Full STA algorithm	- 72 Rx positions	- Hydrophone
Central Frequency	- 3 MHz	- 3.5 MHz	- 7.3 MHz	- 7.5 MHz	- 5 MHz	- 4.7 MHz
Number of CS problems	- 1280	- 7,680	~	-16,384	- 72	~
Spatial resolution	- 0.25 mm - $\lambda/2$	- 0.44 mm - λ	- 0.1 mm - $\lambda/2$	- 0.43 mm - 2λ	~	- 0.03 mm - 0.09λ
Results	- High contrast and spatial resolution - Tissue-mimicking phantom	- 8-fold down-sampling	- High resolution for sparse targets	- Increased frame rate	- Single element imaging	~

of incoherent spatial impulse responses. We demonstrated the successful reconstruction of high-resolution ultrasound images, both in simulation and experimental studies. In the simulation study, the proposed method can achieve a resolution of 0.25 mm, which represents a four-fold improvement over conventional beamforming-based methods. In the experimental study, the proposed method can reconstruct ultrasound images of 0.08-mm-diameter nylon wires. Thus, we have demonstrated that the proposed interference-based method can improve spatial and contrast resolutions.

IV. DISCUSSION

In this section, we compare the results of the proposed method with a few recently published articles. Table II summarizes the differences in terms of the transmit/receive strategy, computational complexity, and resolution. Conventional ultrasound methods require multiple transmissions of the focused ultrasound pulse. For example, a focused B-mode imaging scheme based on delay-and-sum beamforming requires approximately 120 pulse-echo transmissions to reconstruct a single 2-D image. Each pulse-echo transmission

uses up to 128 receiving channels to acquire the RF signals. This results in a large amount of data being processed in real-time. Therefore, Wagner *et al*. [16] proposed a sub-Nyquist sampling scheme based on CS to reduce the amount of data required to reconstruct an ultrasound image. They achieved an eight-fold reduction in the sampling rate by integrating the beamforming process directly with the low-rate sampling process. Likewise, a CS theory was applied to STA imaging in [20] to increase the system's frame rate by reducing the total number of required pulse-echo firings. STA imaging requires 128 firings, one for each element in the transducer array. During the reception, all array elements are used to acquire the reflected ultrasound signals. The full STA data set consists of 16384 RF signals. Liu *et al*. [20] proposed a CS-STA algorithm that could reduce the number of firings from 128 to 32 by combining multiple firings where only 4096 RF signals were acquired. The CS scheme was used to reconstruct the full STA data set with the given 4096 RF signals. This method achieved four-fold data reduction at the cost required to solve 16384 CS problems. High-frame-rate STA imaging can be achieved if all CS problems are solved in real-time. Unlike conventional methods that use delay-and-sum beamforming [16], [20], the proposed interference-based ultrasound does not use any beamforming techniques. Instead, we can directly reconstruct the final ultrasound image's pixel values by finding the correct combination of impulse responses that are present in the measurement signal. Moreover, the 2-D image can be reconstructed using only ten pulse-echo firings. A CS framework derived from the ultrasound propagation theory was described in [21], where a complete ultrasound image can be reconstructed from the transmission of only a single plane wave. This is by far the most relevant work to our proposed interference-based ultrasound method. However, it was reported that the method in [21] could only be used to reconstruct images of sparse objects in the water tank (that consist of few point scatterers) owing to the high coherence in the transmission matrix. In this article, we describe the use of random interference that solves the issue of high coherence in the transmission matrix. Our results show that the proposed method can be used with a tissue-mimicking phantom. Compressed 3-D ultrasound imaging using a single transducer element that features a coded aperture mask was recently proposed in [30]. The acoustic mask is placed in front of the transducer and used to disturb the outgoing ultrasound pulse. Ultrasound signals are acquired at 72 different positions when the coded mask rotates around its axes. The transmission matrix is designed by measuring the spatial impulse responses using a hydrophone and translation stage. The experimental study demonstrates a 3-D ultrasound image of two letters placed in a water tank. Pieter Kruizinga *et al*. [30] achieved a very simple imaging modality by replacing the multielement arrays with a single element transducer. Such an imaging setup can be used to create a portable ultrasound system. However, in this study, we intentionally used an array of transducers to generate random interference because arrays are essential in many other applications such as Doppler imaging, contrast-agent imaging, and high-intensity focused ultrasound ablation. In addition, generating random interference by means of random excitation signals provides greater flexibility for achieving different interference patterns. Furthermore, the mechanical rotation of a physical acoustic lens requires extra time, but the random interference in the proposed method can be changed quickly by using different excitation signals. Clement *et al.* [25] proposed a super-resolution ultrasound imaging technique that utilizes *a priori* measurements of the focused ultrasound pulse in water. Then, the image is reconstructed by finding the best spectral candidate. The results in [25] are impressive which have shown practical applications in transmission-mode imaging such as ultrasound microscopy. Our method is, on the contrary, a reflection-mode imaging and hence is more practical for noninvasive diagnostic applications such as traditional B-mode imaging.

In this work, we have proposed replacing the conventional focused ultrasound pulse with an unfocused ultrasound wavefront of random interference. The proposed method eliminates the need to focus and steer the ultrasound pulse, thereby removing the imposed resolution limit. High-resolution images are reconstructed by identifying spatial impulse responses in the echo signals rather than using the conventional approach of visualizing the strength of echo signals. Simulation and experimental results suggest that ultrasound images can be successfully reconstructed by using an ultrasound wavefront of random interference. In the simulation study, the proposed method achieved a resolution of 0.25 mm, representing a fourfold improvement over conventional beamforming-based methods. In the real phantom experiment, we demonstrated that the proposed method can successfully reconstruct ultrasound images of nylon wires as small as 0.08 mm in diameter using a tissue-mimicking phantom. The proposed interference-based method can be used as general B-mode imaging. In particular, the proposed interference-based method can improve the detection of the boundaries of organs, and the location of lesions in clinical applications such as abdominal and musculoskeletal imaging. In the future, we would like to use a joint reconstruction of the image by taking into account common information across the channels. This will improve reconstruction time and further enhance image resolution.

REFERENCES

[1] A. A. Maznev and O. B. Wright, "Upholding the diffraction limit in the focusing of light and sound," *Wave Motion*, vol. 68, pp. 182–189, Jan. 2017.

[2] A. Ng and J. Swanevelder, "Resolution in ultrasound imaging," *Continuing Educ. Anaesthesia Crit. Care Pain*, vol. 11, no. 5, pp. 186–192, 2011.

[3] T. Szabo, *Diagnostic Ultrasound Imaging: Inside Out*, 2nd ed. Boston, MA, USA: Academic, 2014.

[4] O. T. von Ramm and S. W. Smith, "Beam steering with linear arrays," *IEEE Trans. Biomed. Eng.*, vol. BME-30, pp. 438–452, 1983.

[5] G. Montaldo, M. Tanter, J. Bercoff, N. Benech, and M. Fink, "Coherent plane-wave compounding for very high frame rate ultrasonography and transient elastography," *IEEE Trans. Ultrason., Ferroelectr., Freq. Control*, vol. 56, no. 3, pp. 489–506, Mar. 2009.

[6] J. A. Jensen, S. I. Nikolov, K. L. Gammelmark, and M. H. Pedersen, "Synthetic aperture ultrasound imaging," *Ultrasonics*, vol. 44, pp. e5–e15, Dec. 22, 2006.

[7] J. F. Synnevag, A. Austeng, and S. Holm, "Adaptive beamforming applied to medical ultrasound imaging," *IEEE Trans. Ultrason., Ferroelectr., Freq. Control*, vol. 54, no. 8, pp. 1606–1613, Aug. 2007.

[8] J. Kang, J. Y. Lee, and Y. Yoo, "A new feature-enhanced speckle reduction method based on multiscale analysis for ultrasound B-Mode imaging," *IEEE Trans. Biomed. Eng.*, vol. 63, no. 6, pp. 1178–1191, Jun. 2016.
[9] P. C. Tay, C. D. Garson, S. T. Acton, and J. A. Hossack, "Ultrasound despeckling for contrast enhancement," *IEEE Trans. Image Process.*, vol. 19, no. 7, pp. 1847–1860, Jul. 2010.
[10] I. Trots, Y. Tasinkevych, A. Nowicki, and M. Lewandowski, "Golay coded sequences in synthetic aperture imaging systems," *Arch. Acoust.*, vol. 36, no. 4, pp. 913–926, Jan. 2011.
[11] P. Gong, M. C. Kolios, and Y. Xu, "Delay-encoded transmission and image reconstruction method in synthetic transmit aperture imaging," *IEEE Trans. Ultrason., Ferroelectr., Freq. Control*, vol. 62, no. 10, pp. 1745–1756, Oct. 2015.
[12] D. L. Donoho, "Compressed sensing," *IEEE Trans. Inf. Theory*, vol. 52, no. 4, pp. 1289–1306, Apr. 2006.
[13] R. G. Baraniuk, "Compressive sensing [lecture notes]," *IEEE Signal Process. Mag.*, vol. 24, no. 4, pp. 118–121, Jul. 2007.
[14] E. J. Candes and M. B. Wakin, "An introduction to compressive sampling," *IEEE Signal Process. Mag.*, vol. 25, no. 2, pp. 21–30, Mar. 2008.
[15] N. Wagner, Y. C. Eldar, A. Feuer, G. Danin, and Z. Friedman, "Xampling in ultrasound imaging," *Proc. SPIE*, vol. 7968, Mar. 2011, Art. no. 796818.
[16] N. Wagner, Y. C. Eldar, and Z. Friedman, "Compressed beamforming in ultrasound imaging," *IEEE Trans. Signal Process.*, vol. 60, no. 9, pp. 4643–4657, Sep. 2012.
[17] J. Zhou, S. Hoyos, and B. Sadler, "Asynchronous compressed beamformer for portable diagnostic ultrasound systems," *IEEE Trans. Ultrason., Ferroelectr., Freq. Control*, vol. 61, no. 11, pp. 1791–1801, Nov. 2014.
[18] C. Quinsac, A. Basarab, and D. Kouamé, "Frequency domain compressive sampling for ultrasound imaging," *Adv. Acoust. Vibrat.*, vol. 2012, May 2012, Art. no. 231317.
[19] H. Liebgott, R. Prost, and D. Friboulet, "Pre-beamformed RF signal reconstruction in medical ultrasound using compressive sensing," *Ultrasonics*, vol. 53, no. 2, pp. 525–533, Feb. 2013.
[20] J. Liu, Q. He, and J. Luo, "A compressed sensing strategy for synthetic transmit aperture ultrasound imaging," *IEEE Trans. Med. Imag.*, vol. 36, no. 4, pp. 878–891, Apr. 2017.
[21] G. David, J.-L. Robert, B. Zhang, and A. F. Laine, "Time domain compressive beam forming of ultrasound signals," *J. Acoust. Soc. Amer.*, vol. 137, no. 5, pp. 2773–2784, May 2015.
[22] P. Song, A. Manduca, J. D. Trzasko, R. E. Daigle, and S. Chen, "On the effects of spatial sampling quantization in super-resolution ultrasound microvessel imaging," *IEEE Trans. Ultrason., Ferroelectr., Freq. Control*, vol. 65, no. 12, pp. 2264–2276, Dec. 2018.
[23] P. Song *et al.*, "Improved super-resolution ultrasound microvessel imaging with spatiotemporal nonlocal means filtering and bipartite graph-based microbubble tracking," *IEEE Trans. Ultrason., Ferroelectr., Freq. Control*, vol. 65, no. 2, pp. 149–167, Feb. 2018.
[24] B. Cox and P. Beard, "Imaging techniques: Super-resolution ultrasound," *Nature*, vol. 527, no. 7579, pp. 2–451, Nov. 26 2015.
[25] G. T. Clement, J. Huttunen, and K. Hynynen, "Superresolution ultrasound imaging using back-projected reconstruction," *J. Acoust. Soc. Amer.*, vol. 118, no. 6, pp. 3953–3960, Dec. 2005.
[26] D. Stork, A. Ozcan, and P. R. Gill, "Imaging without lenses," *Amer. Sci.*, vol. 106, no. 1, p. 28, Jan. 2018.
[27] A. Liutkus *et al.*, "Imaging with nature: Compressive imaging using a multiply scattering medium," *Sci. Rep.*, vol. 4, no. 1, p. 5552, May 2015.
[28] H. Jang, C. Yoon, E. Chung, W. Choi, and H.-N. Lee, "Speckle suppression via sparse representation for wide-field imaging through turbid media," *Opt. Express*, vol. 22, no. 13, p. 16619, Jun. 2014.
[29] Y. Choi *et al.*, "Overcoming the diffraction limit using multiple light scattering in a highly disordered medium," *Phys. Rev. Lett.*, vol. 107, no. 2, Jul. 2011, Art. no. 023902.
[30] P. Kruizinga *et al.*, "Compressive 3D ultrasound imaging using a single sensor," *Sci. Adv.*, vol. 3, no. 12, Dec. 2017, Art. no. e1701423.
[31] Y. Xie *et al.*, "Acoustic holographic rendering with two-dimensional metamaterial-based passive phased array," *Sci. Rep.*, vol. 6, no. 1, p. 35437, Dec. 2016.
[32] P. Ni, S. Park, and H.-N. Lee, "Design of unfocused ultrasound imaging system using compressive sensing," presented at the 37th Annu. Int. Conf. IEEE Eng. Med. Biol. Soc. (EMBC), Aug. 25–29, 2015.
[33] M. D. Brown, D. I. Nikitichev, B. E. Treeby, and B. T. Cox, "Generating arbitrary ultrasound fields with tailored optoacoustic surface profiles," *Appl. Phys. Lett.*, vol. 110, no. 9, Feb. 2017, Art. no. 094102.
[34] J. A. Jensen, "Linear description of ultrasound imaging systems," Notes Int. Summer School Adv. Ultrasound Imag., Tech. Univ. Denmark, Lyngby, Denmark, Tech. Rep., Jun. 1999. [Online]. Available: https://orbit.dtu.dk/en/publications/linear-description-of-ultrasound-imaging-systems-notes-for-the-in
[35] J. A. Jensen and N. B. Svendsen, "Calculation of pressure fields from arbitrarily shaped, apodized, and excited ultrasound transducers," *IEEE Trans. Ultrason., Ferroelectr., Freq. Control*, vol. 39, no. 2, pp. 262–267, Mar. 1992.
[36] J. A. Jensen, "FIELD: A program for simulating ultrasound systems," in *Proc. IEEE 10th Nordic-Baltic Conf. Biomed. Imag.*, vol. 34, Mar. 1996, pp. 351–353.
[37] J. F. Yang and Y. Zhang, "Alternating direction algorithms for L1-problems in compressive sensing," *SIAM J. Sci. Comput.*, vol. 33, no. 1, pp. 250–278, 2011.
[38] W. Y. W. Deng and Y. Zhang, "Group sparse optimization by alternating direction method," Rice CAAM, Houston, TX, USA, Tech. Rep. TR11-06, 2011.
[39] S. J. Kim, K. Koh, M. Lustig, S. Boyd, and D. Gorinevsky, "An interior-point method for large-scale ℓ_1-regularized least squares," *IEEE J. Sel. Topics Signal Process.*, vol. 1, no. 4, pp. 606–617, Dec. 2007.
[40] S. S. Chen, D. L. Donoho, and M. A. Saunders, "Atomic decomposition by basis pursuit," *SIAM Rev.*, vol. 43, no. 1, pp. 129–159, Jan. 2001.
[41] S. Park and H.-N. Lee, "Fast mixed integer quadratic programming for sparse signal estimation," *IEEE Access*, vol. 6, pp. 58439–58449, 2018.
[42] A. Nowicki, Z. Klimonda, M. Lewandowski, J. Litniewski, P. A. Lewin, and I. Trots, "Comparison of sound fields generated by different coded excitations—Experimental results," *Ultrasonics*, vol. 44, no. 1, pp. 121–129, Jan. 2006.

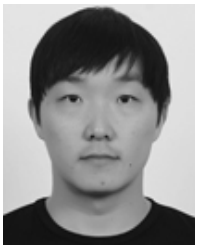

Pavel Ni (Student Member, IEEE) received the B.S. degree in telecommunication technologies from the Tashkent University of Information and Technologies, Tashkent, Uzbekistan, in 2009. He is currently pursuing the M.S./Ph.D. degree with the School of Electrical Engineering and Computer Science, Gwangju Institute of Science and Technology (GIST), Gwangju, South Korea.

His research interests include computational imaging, chaos theory, and deep learning.

Heung-No Lee (Senior Member, IEEE) received the B.S., M.S., and Ph.D. degrees in electrical engineering from the University of California at Los Angeles, Los Angeles, CA, USA, in 1993, 1994, and 1999, respectively.

From 1999 to 2002, he worked as a Research Staff Member with the HRL Laboratories, LLC, Malibu, CA. From 2002 to 2008, he worked as an Assistant Professor with the University of Pittsburgh, Pittsburgh, PA, USA. In 2009, he moved to the School of Electrical Engineering and Computer Science, Gwangju Institute of Science and Technology (GIST), Gwangju, South Korea, where he is currently affiliated. His areas of research include information theory, signal processing theory, communications/networking theory, and their applications to wireless communications and networking, compressive sensing, future internet, and brain–computer interface.

Dr. Lee has received several prestigious national awards, including the Top 100 National Research and Development Award in 2012, the Top 50 Achievements of Fundamental Researches Award in 2013, and Science/Engineer of the Month (January 2014).